ACS APPLIED MATERIALS & INTERFACES

www.acsami.org

Research Article

# Van der Waals Epitaxy of c-Oriented Wurtzite AlGaN on Polycrystalline Mo Substrates for Enhanced Heat Dissipation

Yang Chen, Hang Zang, Shanli Zhang, Zhiming Shi, Jianwei Ben, Ke Jiang, Yuping Jia, Mingrui Liu, Dabing Li, and Xiaojuan Sun*

Cite This: *ACS Appl. Mater. Interfaces* 2022, 14, 37947−37957

Read Online

ACCESS | Metrics & More | Article Recommendations | Supporting Information

**ABSTRACT:** The epitaxy of III-nitrides on metallic substrates is competitive due to the advantages of vertical carrier injection, enhanced heat dissipation, and flexible application in various III-nitride-based devices. However, the serious lattice mismatch, atom diffusion, and interface reaction under the rigorous growth conditions have caused enormous obstacles. Based on the thermal and chemical stability of the graphene layer, we propose the van der Waals epitaxy of c-oriented wurtzite AlGaN on the polycrystalline Mo substrate by high-temperature metal−organic chemical vapor deposition. The insertion of a graphene layer interrupts the chaotic epitaxial relationship between the polycrystalline metal and epilayers, resulting in the single-crystalline orientation along the wurtzite (0002) plane and residual stress release in AlGaN because of the weak van der Waals interaction. We also demonstrate that the epitaxy of AlGaN on Mo metal possesses enhanced heat dissipation ability, in which the epilayer temperature is controlled at only 28.7 °C by the heating of a ∼54 °C hot plate. The heat dissipation enhancement for the present epitaxial structures provides a desirable strategy for the fabrication of efficient ultraviolet devices with excellent stability and lifetime.

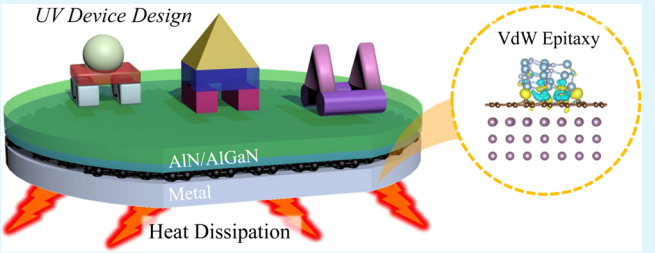


**KEYWORDS:** *AlGaN, Mo substrate, van der Waals epitaxy, MOCVD, heat dissipation*



## INTRODUCTION

The ternary alloy of III-nitrides, AlGaN, possesses large and adjustable direct band gaps ranging from 3.4 to 6.2 eV, and thus it becomes a promising material for detection and luminescence devices working in the ultraviolet (UV) wavelength.[1−3] Peculiarly, the ability of killing most germs and viruses of AlGaN-based deep-UV diodes attracts increasing attention toward this material since the pandemic of COVID-19.[4−8] The nontoxicity of AlGaN and miniaturization and stability of deep-UV diodes compared with traditional mercury lamps further promote demands and advances for AlGaN-related materials.[9] Due to the absence of homoepitaxial substrates, heteroepitaxial substrates including sapphire,[10−12] silicon carbide,[13] and silicon[14,15] are currently applied for AlGaN growth. In addition to the lattice mismatch and thermal expansion coefficient difference between the epilayers and heteroepitaxial substrates, the widely used sapphire also exhibits the drawbacks of mechanical inflexibility, electrical insulation, and poor thermal conductivity (around 2 $W{\cdot}K^{-1}{\cdot}m^{-1}$ for $Al_2O_3$ on sapphire at 200 °C),[16] which prevent the possible application of AlGaN in flexible optoelectronic devices with high efficiency and heat dissipation ability.

Metal is the potential candidate for supporting AlGaN epilayers because of its great ductility and bendability, and high electrical and thermal conductivity ($9.9 \times 10^{-3}$ Ω·cm and 131 $W{\cdot}K^{-1}{\cdot}m^{-1}$ for Mo at 200 °C, respectively),[17] which would result in various applications of AlGaN-based devices with high performance, such as wearable electronics. The epilayer transfer and bonding techniques have provided an opportunity for the integration of AlGaN with metallic substrates.[18,19] In the current "top-down" technique, careful laser lift-off and adhesion layer design are essential,[20] in which maintaining the pristine crystalline quality and achieving the mass production in wafer are difficult. As the solution, a "bottom-up" technical route by direct epitaxy of AlGaN on metallic substrates might be preponderant. However, the high chemical reactivity of the metal induces a serious interface reaction according to the rigorous growth conditions, and the atom diffusion at high temperature further results in the multiple phase separation phenomenon for the epilayers. Moreover, the metal bulk is generally in the polycrystalline state, and thus, the epitaxial relationship depends on the fact that it is challengeable to obtain large-area single-crystalline AlGaN on polycrystalline metals. For instance, Yamada et al. demonstrated that the

Received: June 6, 2022
Accepted: July 28, 2022
Published: August 12, 2022

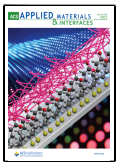




https://doi.org/10.1021/acsami.2c10039
*ACS Appl. Mater. Interfaces* 2022, 14, 37947−37957

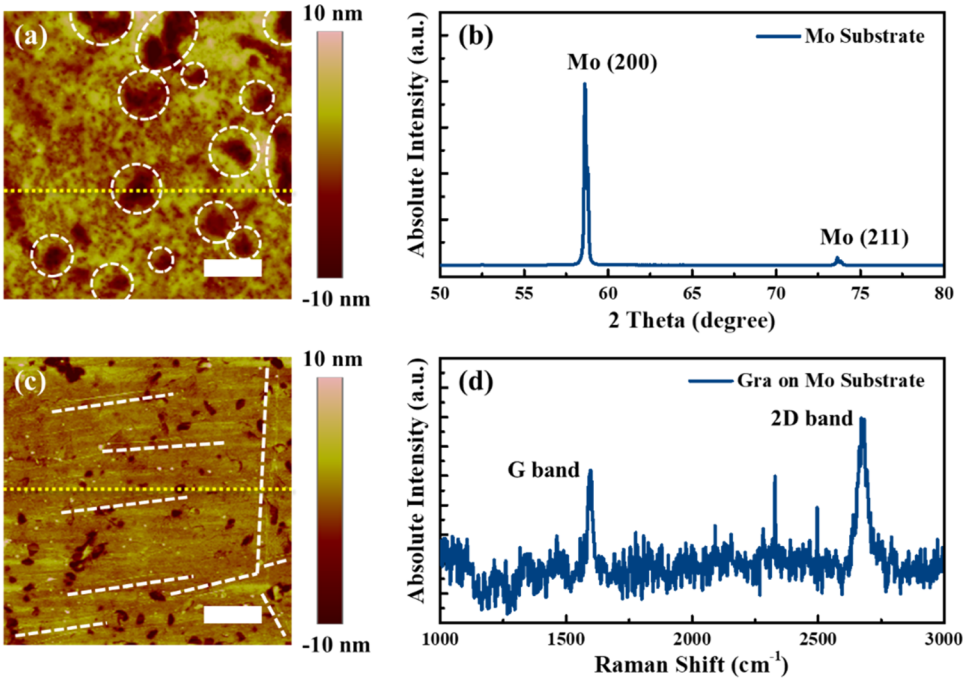


**Figure 1.** (a) AFM images of the Mo substrate and (c) monolayer graphene transferred onto the Mo substrate, which are measured in the tapping mode. (b) Wide-scanning XRD spectra of polycrystalline Mo substrate. (d) Raman spectra of monolayer graphene on the Mo substrate. The yellow dashed lines in (a) and (c) mark the measured position for the height profile. The scale bars in (a) and (c) are 1 $\mu$m.

molecular beam epitaxy of GaN on various high-melting point metals (e.g., Mo, W, and Ta) has polycrystalline properties, and the highest growth temperature is 830 °C.[21]

According to these main obstacles, other previous studies proposed a relatively mild pulsed laser deposition (PLD) method for the epitaxy of Al(Ga)N on single-crystalline metallic substrates.[22−25] Li and co-workers carried out a series of studies by the PLD method, and the growth temperature could be controlled lower than 600 °C.[23−25] At the same time, the single-crystalline metallic substrate provides a stable and consistent epitaxial orientation, which achieves significant improvement for the epilayer crystalline quality. It is to be noted that the relatively low PLD temperature also makes it feasible for low-melting point single-crystalline metals, such as Al(111)[23] and Cu(111),[24] to serve as the epitaxial substrates. Although these efforts promote the advances of bottom-up integration of the Al(Ga)N with metallic substrates, commercial manufacturing might be aborted because of the high cost of inch-scale single-crystalline metals and incompatibility with the widely equipped high-temperature metal−organic chemical vapor deposition (MOCVD) system. We think that the direct encounter with the epitaxy of AlGaN on general polycrystalline metallic substrates by high-temperature MOCVD is imperative, which is one of the most valuable technical routes for the development of AlGaN-based devices. In our previous studies, we utilized two-dimensional materials (e.g., graphene and transition metal disulfide compounds) as the insertion layers for the epitaxy of GaN, realizing enhanced crystalline quality and smaller residual stress due to the weak van der Waals interaction between the epilayers and sapphire substrate.[26,27] The graphene layer exhibits excellent toughness in the high-temperature and reactive gas (e.g., hydrogen and ammonia) atmosphere during the growth of the AlN nucleation layer, which provides insights into the van der Waals epitaxy of AlGaN on the polycrystalline metals.

In the present work, we demonstrate the epitaxy of c-oriented wurtzite $Al_{0.7}Ga_{0.3}N$ on the polycrystalline Mo substrate by inserting a graphene monolayer, and this technical route offers a practical strategy for the integration of AlGaN with metallic substrates with the MOCVD system. Based on the crystallography and surface/cross-sectional morphology measurements, the graphene insertion layer screens the lattice field effect from the polycrystalline Mo substrate and eliminates the interface chemical reaction together with atom diffusion, which results in a highly c-oriented growth of AlGaN. The easy exfoliation of AlGaN epilayers proves the weak van der Waals interaction. The theoretical calculations confirm that the insertion of a graphene layer retains the wurtzite crystalline structure predominantly rather than the cubic one (lower total energy for the wurtzite phase). In addition, a relatively large interaction distance with lower coupling density ensures the independence of AlGaN from the polycrystalline Mo substrate, which essentially solves the hardships of nitride epitaxy on polycrystalline metals at high temperature. The thermal management test exhibits the enhanced heat dissipation ability of AlGaN on the Mo substrate, in which the maximum temperature is only 28.7 °C compared to the 47.9 °C for that on the sapphire substrate, decreasing by about 40%. We consider that the present technical route for the van der Waals epitaxy of AlGaN on polycrystalline metallic substrates would trigger fast advances of next-generation deep-UV electronics with high performance and various functionalities.

## RESULTS AND DISCUSSION

The surface morphology of a cleaned Mo substrate (see the Methods) is measured by atomic force microscopy (AFM), as shown in Figure 1a. Several pits with a diameter and depth of 400−800 and 10−20 nm, respectively, appear in the measured area (circled by the white dashed line), which might be caused


https://doi.org/10.1021/acsami.2c10039
ACS Appl. Mater. Interfaces 2022, 14, 37947−37957

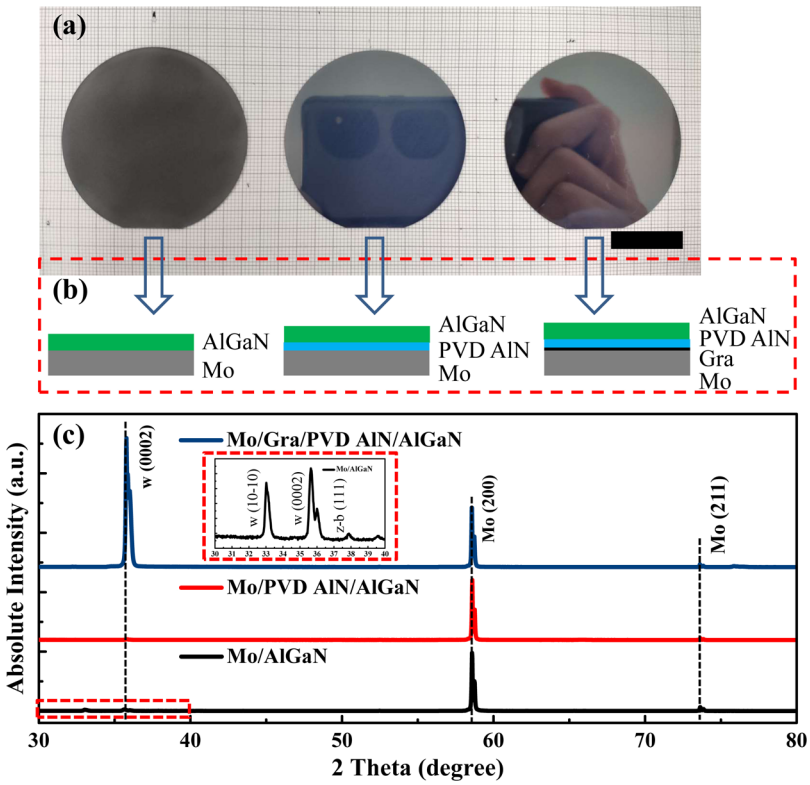


**Figure 2.** (a) Photography and (b) schematic epitaxial structures of three designed samples. (c) Wide-scanning XRD spectra of the AlGaN epilayers shown in (a) and (b). The inset of (c): the enlarged XRD spectra of AlGaN grown on the bare Mo substrate. The scan angle ranges from 30 to 40°. The scale bar in (a) is 2 cm.

by the insufficient polishing technique. In this way, the root-mean-square roughness ($R_q$) of the Mo substrate reaches up to 2.96 nm. As a comparison with Yamada's work, this value is slightly higher than the reported roughness of 1−2 nm for W and Mo substrates.[21] We consider that additional solution etching and annealing treatment would improve the surface flatness of metallic substrates, and it is demonstrated in Figure S1 of the Supporting Information that the $R_q$ of the Mo substrate decreases to 1.86 nm after 10% HCl disposition and annealing at 1000 °C for 1 h. The crystallographic properties of the Mo substrate are evaluated by X-ray diffraction (XRD), as shown in Figure 1b. The preferred diffraction peaks of the Mo(200) plane at 58.6° and Mo(211) plane at 73.6° are both observed, indicating that the Mo substrate possesses a polycrystalline nature.[21]

The AFM image of the graphene layer transferred onto the Mo substrate in Figure 1c exhibits a smoother surface morphology with a reduced $R_q$ of 2.28 nm as the comparison with the pristine Mo substrate, and both pit depth and size decrease after the graphene coverage, which are verified by their height profiles in Figure S2 of the Supporting Information. As marked by the white dashed line, a few graphene wrinkles are generated during the wet transfer process, and no obvious residual polymer is left on the graphene (see the Methods), which is crucial for preventing the following AlGaN from causing residual polymer pollution. The Raman spectra in Figure 1d further illustrate the properties of the graphene layer transferred onto the Mo substrate. The intensity of the defect-related D band ($I_D$) located at ∼1350 $cm^{-1}$ is negligible, demonstrating its high crystalline quality. The intensity ratio of 2D and G bands ($I_{2D}/I_G$) is calculated as 1.55, which is lower than that of the typical monolayer graphene (∼2) transferred onto the dielectric substrates.[28,29] As shown in Figure S3, an identical graphene layer transferred onto the sapphire substrate exhibits an increased $I_{2D}/I_G$ of 2.26, and this difference might be induced by the charge transfer between graphene and metallic substrates,[30] which also appeared in our previous work with the Au film deposited on the monolayer graphene.[31]

Based on the AlGaN epitaxial processes (see the Methods), we design three types of epitaxial structures for comparison. As shown in Figure 2a,b, the Mo, Mo/physical vapor deposition (PVD) AlN, and Mo/graphene (Gra)/PVD AlN serve as the substrates for the epitaxy of AlGaN with the high-temperature MOCVD system. There is a gradually varied tendency in the reflection ability among the three samples after the epitaxy of AlGaN, which represents the interfacial flatness and uniformity between the epilayers and Mo substrate. Compared with the mirror-like Mo substrate in Figure S4 of the Supporting Information, the direct epitaxy of AlGaN on the Mo substrate (left, Figure 2a) destroys its reflection property to a significant degree. We consider that the rigorous interface reaction and atom diffusion between the epilayer and Mo substrate result in interface destruction, which would be verified in the following cross-sectional morphology analysis. Although the predeposition of the PVD AlN on Mo improves the reflection ability (middle, Figure 2a), it still has obvious deficiency compared to the van der Waals epitaxy of AlGaN on the Mo/Gra/PVD AlN (right, Figure 2a), in which the later one exhibits a similar reflection ability of the bare Mo substrate.

The preferred crystalline orientations of AlGaN on different substrates are examined by XRD, as shown in Figure 2c. All the samples exhibit the typical diffraction peaks of the Mo(200) and Mo(211) planes from the Mo substrate underneath, which


https://doi.org/10.1021/acsami.2c10039
ACS Appl. Mater. Interfaces 2022, 14, 37947−37957

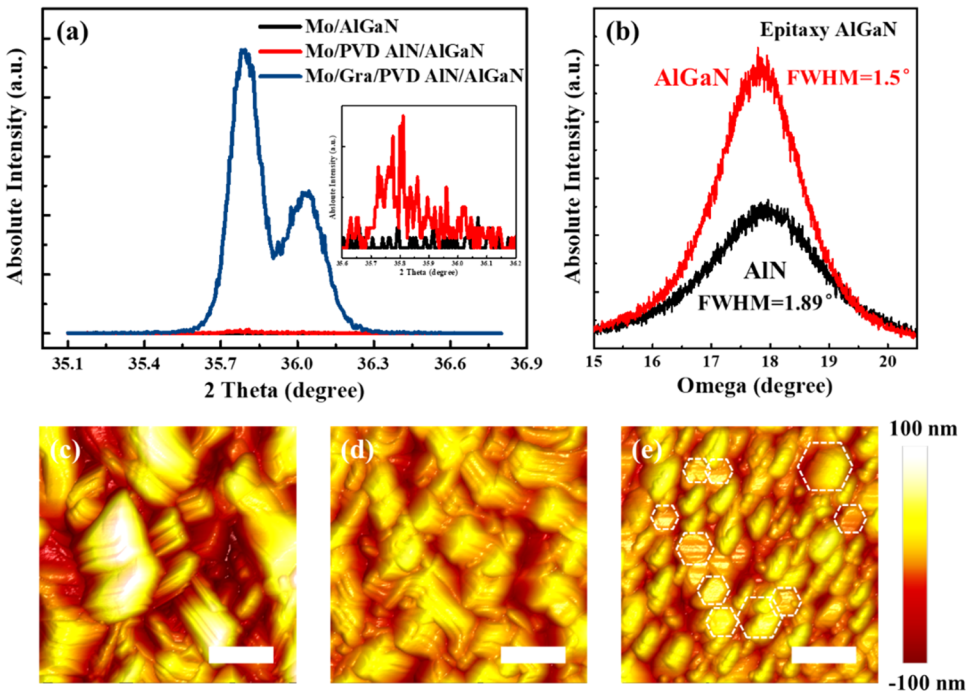


**Figure 3.** (a) Fine-scanning XRD along the wurtzite AlGaN w(0002) plane. The inset of (a): the enlarged spectra for the epitaxy of AlGaN on the Mo and Mo/PVD AlN. (b) XRD rocking curve along the w(0002) of AlN and AlGaN for the van der Waals epitaxy on the Mo/Gra/PVD AlN. (c) AFM images of AlGaN on the Mo, (d) Mo/PVD AlN, and (e) Mo/Gra/PVD AlN, which are measured in the tapping mode. The scale bars in (c)−(e) are 500 nm.

are identical with those of the pristine Mo substrate (see Figure 1b). In this way, it could be deduced that the interfacial destruction of the Mo substrate by the direct epitaxy of AlGaN terminates at a tiny depth compared to its entire thickness (430 $\mu$m), and thus, it ensures that the Mo substrate maintains the pristine crystalline plane in the later XRD measurement. However, the diffraction peak intensity of Mo/AlGaN and Mo/PVD AlN/AlGaN along the wurtzite (0002) [w(0002)] plane is extremely weak, exhibiting over 36 times and 72 times deduction compared with the intensity of the Mo(200) plane. The inset in Figure 2c shows the enlarged XRD spectra of Mo/AlGaN at the range of 30−40°; typical wurtzite ($10\bar{1}0$) [w($10\bar{1}0$)], w(0002), and zinc blende (111) [z-b(111)] plane diffraction peaks are observed for the AlGaN epilayer.[32,33] These results demonstrate that the direct epitaxy of AlGaN on the polycrystalline Mo substrate results in a chaotic crystalline orientation and blended crystalline phase. For the van der Waals epitaxy of AlGaN on the Mo/Gra/PVD AlN, its w(0002) plane diffraction peak intensity significantly exceeds that of the Mo(200) plane, and none of the other diffraction peaks are observed. In this way, the insertion of the graphene layer plays a key role in the epitaxy of c-oriented wurtzite AlGaN.

Fine-scanning XRD along the w(0002) plane is carried out in Figure 3a, which ranges from 35.1 to 36.8°. The tendency of the diffraction peak intensity is similar to the results in Figure 2c, and the weak diffraction peak intensity of AlGaN on the Mo and Mo/PVD AlN substrates is exhibited in the inset of Figure 3a. AlGaN on Mo/Gra/PVD AlN has double peaks located at 35.8 and 36.03°, corresponding to the AlGaN and the AlN epilayers underneath, respectively (see the Methods). The XRD (0002) rocking curves (RC) of AlN and AlGaN on the Mo/Gra/PVD AlN are shown in Figure 3b. The RC full width at half maximum (FWHM) for AlN and AlGaN is 1.89 and 1.5°, respectively. The inserted AlN/AlGaN superlattices (see the Methods) have suppressed the dislocations extending from the AlN into the AlGaN epilayer, resulting in a higher crystalline quality. It is to be noted that the RC values of Mo/AlGaN and Mo/PVD AlN/AlGaN are undetectable due to their poor crystalline quality, which is also confirmed by the wide-scanning XRD in Figure 2c. The optical property of AlGaN is evaluated by photoluminescence (PL) spectra in Figure S5 of the Supporting Information, and they are fitted into peaks with Lorentzian functions. For the Mo/PVD AlN/AlGaN and Mo/Gra/PVD AlN/AlGaN, two peaks of near band-edge transition (peak 1 locates at ∼232 nm) and radiative recombination of a shallow donor with a valence band (peak 2 locates at ∼236 nm) are observed. The strong near band-edge emission of AlGaN with the graphene insertion layer identifies its higher crystalline quality, and the position of peak 1 corresponds to the Al content of 70%. However, only one weak peak at ∼248 nm appears for Mo/AlGaN, which might be induced by the radiative recombination via the relatively deeper level due to a large number of defects in AlGaN, and thus, its poor crystalline quality results in the absence of AlGaN near band-edge emission.

The Raman spectra of Mo/AlGaN, Mo/PVD AlN/AlGaN, and Mo/Gra/PVD AlN/AlGaN are shown in Figure S6a of the Supporting Information, and the measured range of 300−1000 $cm^{-1}$ covers the main bands of AlGaN. The typical Raman $A_1$ (TO), $E_2$, and $E_1$ (LO) modes of Mo/Gra/PVD AlN/AlGaN are located at 612.4, 657.4, and 888.8 $cm^{-1}$, respectively, and these modes also appear in the AlGaN on Mo and Mo/PVD AlN. Here, we notice that the GaN-like Raman mode appears in Mo/AlGaN (at 581.8 $cm^{-1}$), which might be induced by the crystal component segregation from AlGaN. The $E_2$ mode of AlGaN is very sensitive to residual stress, which could be described as $\sigma = K \times \Delta E_2$, in which $\Delta E_2$ refers to the difference


https://doi.org/10.1021/acsami.2c10039
ACS Appl. Mater. Interfaces 2022, 14, 37947−37957

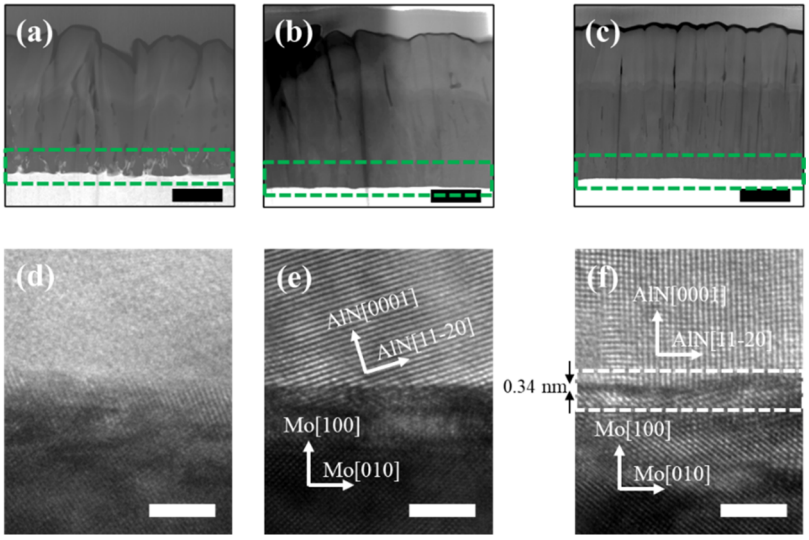


**Figure 4.** Cross-sectional TEM images of (a) Mo/AlGaN, (b) Mo/PVD AlN/AlGaN, and (c) Mo/Gra/PVD AlN/AlGaN. The epitaxial interface is marked by the green dashed line. (d)−(f) High-resolution TEM (HRTEM) of the epitaxial interface in (a)−(c), respectively. The scale bars in (a)−(c) are 500 nm, and those in (d)−(f) are 2 nm.

of the $E_2$ band position with respect to the stress-free one (located at 657.4 $cm^{-1}$) and $K$ is a stress coefficient of ∼2.56 $cm^{-1}·GPa^{-1}$.[34] As shown in Figure S6b of the Supporting Information, the residual stress values of AlGaN on Mo, Mo/PVD AlN, and Mo/Gra/PVD AlN are calculated to be 2.3, 1.5, and 0.1 GPa, respectively. Hence, the residual stress in the AlGaN epilayer is nearly eliminated by the insertion of the graphene layer due to its weak van der Waals interaction, which is consistent with the previous studies for the van der Waals epitaxy of Al(Ga)N on the sapphire substrate.[34,35]

The surface morphology of these samples is characterized by AFM, as shown in Figure 3c−e. The surface morphology could be divided into two types on the basis of the XRD crystalline properties in Figure 2c. As for the AlGaN epitaxy on Mo and Mo/PVD AlN, the rhombohedron-shaped morphology is predominant in the measured area, while Mo/AlGaN possesses a relatively larger size in structures. In addition, the minor structures have filled in the crevices among rhombohedral "islands", showing the probable coexistence of zinc blende and wurtzite-phase AlGaN structures.[36] The $R_q$ of Mo/AlGaN and Mo/PVD AlN/AlGaN is 38.7 and 19.9 nm, respectively. With the insertion of the graphene layer, the AlGaN surface morphology transforms into typical hexagonal wurtzite structures, as marked by the white dashed line in Figure 3e. The decreased surface roughness ($R_q$ = 17.6 nm) and crystalline structure transformation indicate the c-oriented growth of wurtzite AlGaN by the van der Waals epitaxy process. These surface morphology properties are further confirmed by scanning electron microscopy (SEM) in Figure S7 of the Supporting Information, revealing the coincident structural morphology and variation tendency.

The interfacial reaction and atom diffusion at the epitaxial interface of the Mo substrate and epilayers are primarily evaluated by cross-sectional transmission electron microscopy (TEM) in Figure 4a−c. The direct epitaxy of AlGaN at high temperature would trigger the easy chemical reaction of the Mo substrate, and the rough and indistinct interface morphology suggests that atom diffusion has occurred (see Figure 4a). This is proved by the energy dispersive X-ray (EDX) maps of Mo and Al atom distributions at the epitaxial interface, showing obvious Mo atom diffusion into the AlN grain boundaries, which extends to a distance of over 300 nm, as shown in Figure S8a−c of the Supporting Information. Although the predeposition of a low-temperature PVD AlN layer partly improves the interface properties (see Figure 4b), it is inferior to the epitaxy with graphene insertion; the later possesses a smooth and clear interface boundary (see Figure 4c). At the same time, the EDX maps at the epitaxial interface with graphene insertion have no obvious metal atom diffusion, indicating that the graphene layer could effectively suppress the undesired interfacial atom diffusion and chemical reaction during the high-temperature epitaxy process by MOCVD, as shown in Figure S8d−f of the Supporting Information.

The epitaxial relationship between the Mo substrate and AlN for these three designed samples is investigated by cross-sectional high-resolution TEM (HRTEM) at their epitaxial interface, as shown in Figure 4d−f. For the direct epitaxy of AlGaN on the Mo substrate, the serious diffusion of Mo atoms and chemical reaction at the interface would result in the disordered atom arrangement and poor crystalline quality. Hence, in Figure 4d, the lattice is indistinct for both the Mo substrate and epilayer. Partial modification of the epitaxial interface using a low-temperature PVD AlN layer makes the epitaxial relationship clear, but the lattice of PVD AlN has inherited the Mo[100] underneath, inducing a deviation of the AlN[0001] orientation from the epitaxial direction by around 17°, as shown in Figure 4e. This would cause hindrance for the epitaxy on the polycrystalline Mo substrate since the tight epitaxial relationship triggers similar chaotic crystalline orientations in AlGaN. After inserting a graphene layer, the epitaxial relationship changes into Mo[100]//AlN[0001], which is consistent with the XRD results in Figure 2c. As marked by the white dashed lines in Figure 4f, there is a gap of 0.34 nm between the Mo substrate and AlN, corresponding to the thickness of monolayer graphene. The change in the epitaxial relationship demonstrates that the graphene layer breaks the Mo lattice field effect on the epilayer, in which the epitaxial process is mainly controlled by the graphene layer. Therefore, the van der Waals epitaxy of AlGaN is in the


https://doi.org/10.1021/acsami.2c10039
ACS Appl. Mater. Interfaces 2022, 14, 37947−37957

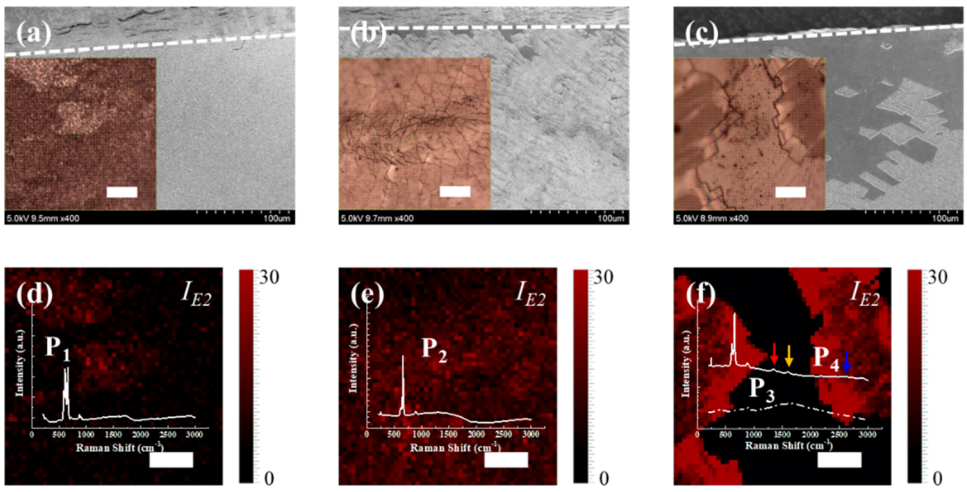


**Figure 5.** (a)−(c) Top-view SEM images at the AlGaN surface near the cutting boundary. The insets of (a)−(c): the corresponding OM images. The scale bars are 20 $\mu$m. (d)−(f) Raman mapping of $E_2$ band intensity for the AlGaN samples in (a)−(c). The insets of (d)−(f): typical Raman spectra of the selected position in the Raman mapping. The scale bars in (d)−(f) are 20 $\mu$m.

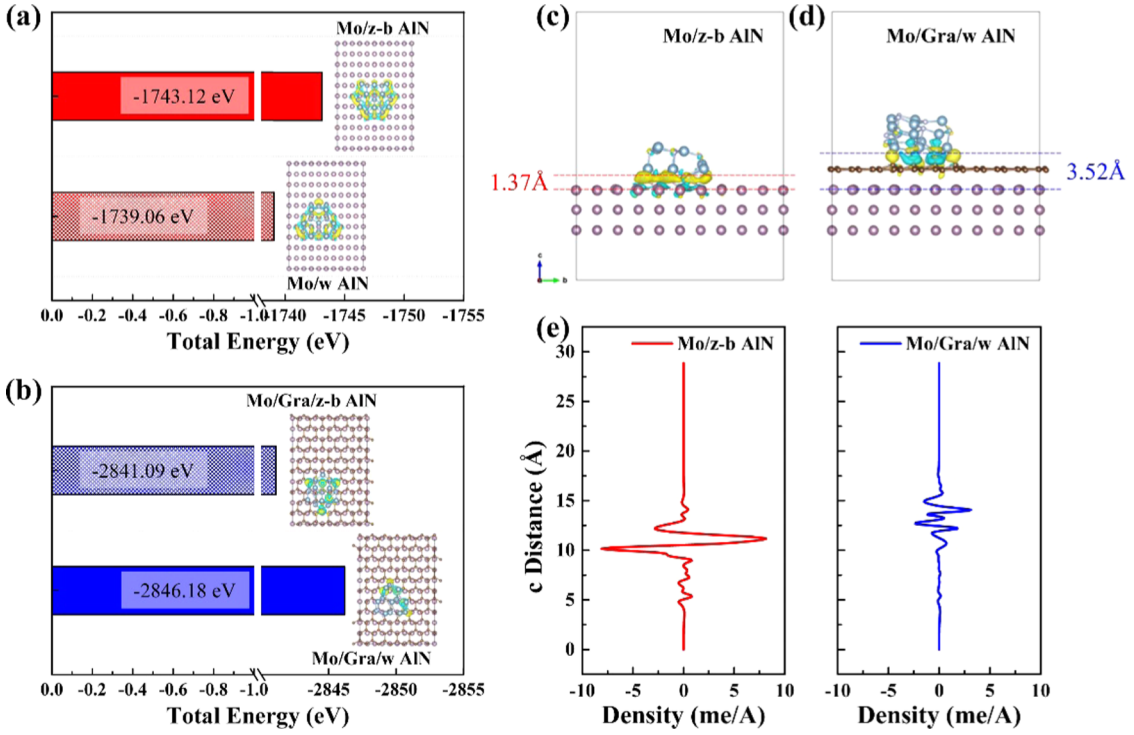


**Figure 6.** (a) Total energy of z-b AlN and w AlN on Mo(200) and (b) Mo(200)/Gra. The insets of (a) and (b): top-views of schematic stacked structures. (c) Cross-sectional stacked structures of z-b AlN on Mo(200) and (d) w AlN on Mo(200)/Gra with the interaction distance and density distribution mapping. (e) Density distribution curve along the epitaxial direction extracted from (c) and (d).

preferred c-orientation despite the metallic substrate with a polycrystalline nature.

The ductile abilities of the metallic Mo and the AlGaN epilayer have a huge difference; therefore, the mechanical deformation at the boundaries of the Mo substrate induced by the cutting process (see the Methods) generates stress in AlGaN epilayers, which could not be released by deformation according to its rigidity. In the other release approach, the formation of cracks is exhibited in the top-view SEM images in Figure 5a−c. In Figure 5a, no epilayer crack is observed for Mo/AlGaN, and it might be attributed to the strong interaction of the integrated interface between the Mo substrate and AlGaN epilayer. The cracks of AlGaN epilayers are subsistent on both the Mo/PVD AlN and Mo/Gra/PVD AlN (see Figure 5b,c), but large-area epilayer exfoliation only occurs when the graphene layer is inserted. These results demonstrate that the graphene insertion layer plays a key role in providing weak van der Waals interaction during the epitaxy of AlGaN.

The crack and exfoliation of AlGaN epilayers are further confirmed by optical microscopy (OM) and Raman mapping, as shown in the insets of Figure 5a−f, respectively. The OM images are similar to the results obtained by SEM, and the corresponding Raman mapping of $E_2$ intensity ($I_{E_2}$) also


https://doi.org/10.1021/acsami.2c10039
ACS Appl. Mater. Interfaces 2022, 14, 37947−37957

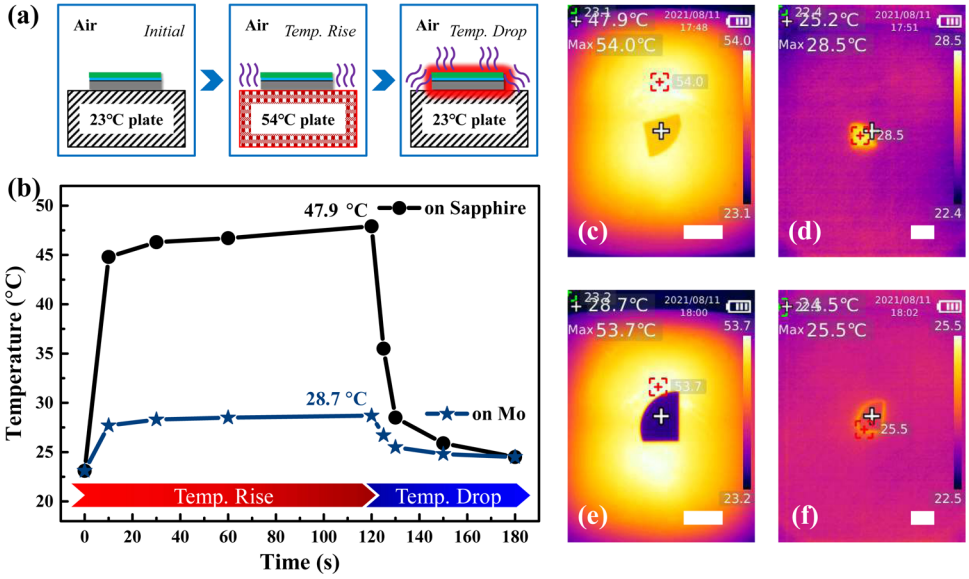


**Figure 7.** (a) Schematic diagram of the heat dissipation measurement for the van der Waals epitaxy of AlGaN on the Mo and sapphire substrates. (b) Temperature as a function of time corresponding to the measurement in (a), and the rise and drop times are 120 and 60 s, respectively. (c) Thermal imaging of AlGaN on the sapphire substrate at the time of 120 s and (d) 180 s. (e) Thermal imaging of AlGaN on the Mo substrate at the time of 120 s and (f) 180 s. The scale bars in (c)−(f) are 1 cm.

demonstrates the partial breakage of AlGaN on Mo/Gra/PVD AlN. As the color scale bar for the intensity is in an identical and equivalent variation (0−30 au), the brightest red color in Figure 5f represents the strongest $I_{E_2}$ for the van der Waals epitaxy of AlGaN on Mo/Gra/PVD AlN corresponding to the highest crystalline quality. We extract the typical Raman spectra (at the range of 200−3000 $cm^{-1}$) from the Raman mapping, as shown in the insets of Figure 5d−f. The scan range of Raman spectra covers the main bands of both the AlGaN and the graphene layer. The exfoliated and retained AlGaN positions in Figure 5f are named as $P_3$ and $P_4$, respectively. At position $P_4$, both the AlGaN and graphene bands appear. The enlarged graphene-related bands at the range of 1000−3000 $cm^{-1}$ in Figure S9 of the Supporting Information exhibit the strong D and D′ peaks related to the defects of graphene, and it might be attributed to the local C−N bonding in graphene during the AlGaN epitaxy process, which is also observed in our previous work.[26] The bonding between the epilayer and graphene is further confirmed by the Raman spectra of the exfoliated region at $P_3$, in which no bands of graphene are found due to the simultaneous exfoliation of AlGaN epilayers and graphene layer. To confirm the initial influence on the structural properties of graphene by PVD AlN deposition, the Raman spectra of Mo/Gra/PVD AlN are measured in Figure S10 of the Supporting Information. Compared with the Raman spectra of pristine graphene in Figure 1d, the enhanced intensity of the D band reveals that the C−N bonding is generated early by the growth of PVD AlN. It is to be noted that the whole intensity of graphene bands decreases for that after the AlGaN epitaxy process, inset of Figure 5f, which is induced by the harder Raman signal collection of graphene through the later epitaxial structures with a larger layer thickness.

According to the XRD results in Figure 1b, the much stronger Mo(200) diffraction peak compared with that of the Mo(211) plane indicates that the Mo(200) plane is dominated in the polycrystalline Mo substrate. Considering that the AlN layer is first deposited on the substrate either by the PVD or MOCVD method, we carry out the theoretical calculations of AlN nuclei on Mo(200) and Mo(200)/Gra by density functional theory (see the Methods). As shown in Figure 6a,b, the AlN nuclei with zinc blende (z-b) and wurtzite (w) phases are placed on Mo(200) and Mo(200)/Gra, respectively. The calculated total energy for Mo/z-b AlN and Mo/w AlN is −1743.12 and −1739.06 eV, respectively, in which the Mo/z-b AlN structure exhibits a energy decreased by 4.06 eV. In addition, the total energy of w AlN on Mo/Gra (−2846.18 eV) decreases by 5.09 eV compared to that of z-b AlN on Mo/Gra (−2841.09 eV). The lower total energy corresponds to a more stable structure; in this way, z-b AlN is preferred on Mo, while w AlN is preferred on Mo/Gra. It is consistent with the experimental results exhibited in Figures 2 and 3, in which the insertion of a graphene layer results in the c-oriented wurtzite AlGaN epitaxy. However, we also noticed that there is a slight difference in the epitaxy of AlN on Mo in theoretical and experimental results. The experimental coexistence of z-b and w-phase Al(Ga)N in spite of the total energy difference is reasonable since the real epitaxy process is complicated (e.g., the interfacial reaction and atom diffusion of the Mo substrate are not considered in the present calculations). Moreover, the z-b AlN belongs to the metastable phase compared with the w AlN, and thus, z-b AlN might transform into the other phase during the growth process.[37]

Figure 6c,d shows the cross-sectional diagram of the stable Mo/z-b AlN and Mo/Gra/w AlN structures, respectively. The interaction distance between Mo and AlN nuclei is calculated as 1.37 Å, and this value increases nearly 3 times (3.52 Å) after the insertion of the graphene layer. The remote interaction would weaken the lattice field effect from the Mo substrate underneath, which is revealed by the interfacial density distribution. As shown in Figure 6e, the density distribution curves along the epitaxial direction are extracted from the density mapping in Figure 6c,d. When the AlN nuclei directly come into contact with the Mo substrate (Figure 6c and left in Figure 6e), a high concentration of density emerges at the


https://doi.org/10.1021/acsami.2c10039
ACS Appl. Mater. Interfaces 2022, 14, 37947−37957

interface of the Mo substrate and AlN nuclei, resulting in the inevitable chemical reaction and atom diffusion. In the configuration with the insertion of the graphene layer, the concentration of density is suppressed and mainly locates at the interface of graphene and AlN nuclei. The absence of density between Mo and Gra/AlN indicates that graphene screens the lattice field effect from the Mo substrate, and the epitaxy process is controlled by the graphene layer, corresponding to the van der Waals epitaxy as a reference to the Al(Ga)N on the single Mo substrate. According to the large lattice mismatch (~14%) between the AlN and Mo substrate in Figure S11 of the Supporting Information, the screening of the Mo lattice field effect by inserting a graphene layer would relieve the generation of dislocation in the AlGaN epilayer.

To evaluate the heat dissipation ability, the identical van der Waals epitaxy of AlGaN on the sapphire substrate is carried out as a comparison, and the measurement is illustrated in Figure 7a. This measurement consists of a thermal absorption process of placing the 23 °C sample on a ~54 °C hot plate and a thermal release process by removing the hot plate, and the persistent time for these two processes is 120 and 60 s, respectively (see the Methods). As shown in Figure 7b, the temperature at critical timelines is plotted, and the thermal imaging of AlGaN on the sapphire and Mo substrates at 120 and 180 s is presented in Figure 7c–f, respectively. The maximum temperatures are located at the time of 120 s, corresponding to 47.9 °C (on sapphire) and 28.7 °C (on Mo). In the present configuration, the excellent thermal conductivity of the metallic Mo substrate provides a high-throughput pathway of heat dissipation from the AlGaN into the surroundings, resulting in less thermal accumulation in the AlGaN epilayer compared with that on the sapphire substrate. Furthermore, the excellent heat dissipation ability of AlGaN on the Mo substrate is confirmed by controlling the temperature of the hot plate at the range of 46.8–114.8 °C, and the maximum temperature (after 120 s on the hot plate) as a function of the hot plate temperature is plotted in Figure S12a of the Supporting Information, in which the thermal imaging is also exhibited. The AlGaN on the Mo substrate has a consistently lower temperature compared with that on the sapphire substrate, especially for the hot plate with the highest temperature of 114.8 °C, and the maximum temperature of AlGaN on the Mo substrate (46.7 °C) decreases by ~52% in contrast with that on the sapphire substrate (97.7 °C). We believe that the enhanced heat dissipation ability of AlGaN is significant for the fabrication of high-performance UV devices with longer lifetime and persistent stability.

## CONCLUSIONS

In conclusion, the van der Waals epitaxy of c-oriented wurtzite AlGaN on the polycrystalline Mo substrate is achieved by the insertion of a graphene layer. Here, the graphene layer screens the lattice field effect from polycrystalline Mo substrates, successfully suppressing the interface reaction and atom diffusion during the high-temperature growth process by MOCVD. The AlGaN with a Al content of 0.7 presents only one diffraction peak related to the w(0002) plane and hexagonal crystalline grain alignment with improved surface morphology; at the same time, the residual stress is dramatically released according to the position of the Raman $E_2$ band. Both the easy exfoliation of AlGaN and results of theoretical calculations demonstrate the weak van der Waals interaction, which promotes the epitaxy of the single-crystalline phase and stress-free AlGaN materials. The outstanding heat dissipation ability for the AlGaN epilayer on the Mo substrate is confirmed by the lower maximum temperature of 28.7 °C on a ~54 °C hot plate. The present work offers a feasible strategy for the direct epitaxy of AlGaN on polycrystalline metallic substrates under rigorous conditions, and it is one of the key preconditions for advances in functional AlGaN-based deep-UV devices with high performance.

## METHODS

**Substrate Preparation and van der Waals Epitaxy of AlGaN.** The 2 inch double-polished Mo substrate with a thickness of 430 μm was purchased from a commercial supplier. Then, the Mo substrate was ordinally ultrasonically cleaned using acetone, ethanol, and deionized water and dried using a nitrogen gun and 95 °C drying case. The monolayer graphene was first synthesized on catalytic Cu foils using a low-pressure chemical vapor deposition system. 200 sccm Ar served as the carrier gas, and 3 sccm $CH_4$ and 100 sccm $H_2$ reacted at 1000 °C to produce C species. The growth process was maintained for 40 min with consistent $CH_4$ input and rapidly cooled to room temperature by removing the heating furnace. After that, the graphene on Cu foils was transferred onto Mo substrates by a polymer-supported wet transfer method. Initially, about 1 μm polymer (S1805G) was coated onto the Cu foil/graphene, and the graphene on the backside of Cu foils was destroyed using Ar plasma. Then, the Cu foil was etched using $Na_2(SO_4)_2$, leaving the graphene/polymer membrane floating on the surface of the solution. After cleaning using deionized water twice, it was transferred onto the foreign substrates and dried in air. At last, the polymer was dissolved in 85 °C acetone, retaining graphene on the target substrate.[38] For the high-Al content AlGaN epitaxy, a 200 nm AlN was first deposited onto the substrate by the PVD method. Then, the high-temperature MOCVD system was applied for the following growth, and trimethylaluminum (TMAl), trimethylgallium (TMGa), and ammonia ($NH_3$) are supplied as the sources of Al, Ga, and N atoms, respectively. At the beginning, the AlN was grown at 1150 °C for 30 min with a pressure of 30 mbar and V/III ratio of 2.8. After that, the 10-loop AlN/AlGaN superlattice was deposited by alternately switching the TMGa source at a consistent temperature and pressure of 1155 °C and 50 mbar, respectively; the source flux values for TMAl, TMGa, and $NH_3$ were set as 120, 20, and 800 sccm, respectively. Following the last loop in the AlN/AlGaN superlattice, the AlGaN epilayer with a thickness of about 1 μm was grown for 1 h, in which the growth parameters are the same as the AlGaN in the superlattice.

**Theoretical Calculations.** Density functional theory calculations are performed using the Vienna ab initio simulation package (VASP).[39,40] The interaction between the core and valence electrons is described with the frozen-core projector augmented wave (PAW) approach.[41,42] The electronic structure is calculated with the Perdew–Burke–Ernzerhof (PBE)[43] functional. The DFT-D3 correction[44] is adopted to describe the long-range van der Waals interaction. An energy cutoff of 400 eV is employed, and spin polarization is considered for all the calculations. The atomic positions are optimized using the conjugate gradient scheme until the maximum force on each atom is less than 0.02 eV $Å^{-1}$. The Mo(200) surface is modeled using as a three-layer rectangular slab; the lattice lengths of the rectangular slab along the surface are 15.8 and 22.4 Å. A vacuum space greater than 20 Å perpendicular to the Mo(200) surface is applied to separate the interactions between neighboring slabs. A γ-only k-mesh is adopted for this model to sample the Brillouin zone. During the structure optimization process, the bottom two layers are fixed with the bulk atomic position, and the top layer is free to relax. The AlN nuclei with wurtzite and zinc blende structures are placed on the bare Mo(200) surface and Mo(200)/graphene surface to study the relative stability; the corresponding charge redistribution is obtained by $\Delta\rho = \rho_{total} - \rho_{Mo} - \rho_{AlN}$ and $\Delta\rho = \rho_{total} - \rho_{Mo/graphene} - \rho_{AlN}$.


https://doi.org/10.1021/acsami.2c10039
ACS Appl. Mater. Interfaces 2022, 14, 37947–37957

**Materials and Thermal Management Characterizations.** Powder (D8 Focus, Bruker) and thin-film X-ray diffractometers (D8 Discover, Bruker) were applied for the crystallography research. An atomic force microscope (Multimode 8, Bruker), scanning electron microscope (S-4800, Hitachi), and transmission electron microscope (Tecnai G2 F20 S-TWIN, FEI) were used to evaluate the surface/cross-sectional morphology. For the sample separation, the 2 inch sample was cut into 5 × 5 $mm^2$ pieces using a tinsmith snip, and the cross-section was polished using fine emery paper. The Raman spectra and mapping data were collected using a Raman spectrometer (LabRAM HR Evolution, HORIBA Scientific) with an excitation laser wavelength and intensity of 520 nm and 25%, respectively, and the scanning step of Raman mapping is controlled at 1 $\mu$m. The photoluminescence spectra of AlGaN were collected using a spectrometer with 220 nm laser excitation at room temperature. A hot plate with the varied temperature of 46.8−114.8 °C was used as the heat source, which is standardized using an infrared imager (UTI220A Pro, UNI-T). The heat dissipation ability test is made up of two processes, including a heat absorption section by placing the sample onto the hot plate for 120 s and a heat release section by removing the hot plate for 60 s. The corresponding temperatures at typical timelines were measured using the infrared imager for the heat dissipation comparison of the van der Waals epitaxy of AlGaN on sapphire and Mo substrates.

## ■ ASSOCIATED CONTENT

### Supporting Information

The Supporting Information is available free of charge at https://pubs.acs.org/doi/10.1021/acsami.2c10039.

> Surface morphology of the Mo substrate after optimization, height profiles of the Mo substrate before and after graphene coverage, Raman spectra of graphene on the sapphire substrate, image of the pristine Mo substrate, PL spectra, Raman spectra and SEM images of AlGaN epilayers, metal species distribution at the epitaxial interface, enlarged Raman spectra at $P_3$ and $P_4$, Raman spectra of Mo/Gra/PVD AlN, lattice constant of Mo and AlN, and heat source-dependent maximum temperature variation of AlGaN (PDF)

## ■ AUTHOR INFORMATION


### Corresponding Author

**Xiaojuan Sun** − *State Key Laboratory of Luminescence and Applications, Changchun Institute of Optics, Fine Mechanics and Physics, Chinese Academy of Sciences, Changchun 130033, China; Center of Materials Science and Optoelectronics Engineering, University of Chinese Academy of Sciences, Beijing 100049, China;* orcid.org/0000-0001-6836-3893; Email: sunxj@ciomp.ac.cn

### Authors

**Yang Chen** − *State Key Laboratory of Luminescence and Applications, Changchun Institute of Optics, Fine Mechanics and Physics, Chinese Academy of Sciences, Changchun 130033, China; Center of Materials Science and Optoelectronics Engineering, University of Chinese Academy of Sciences, Beijing 100049, China*

**Hang Zang** − *State Key Laboratory of Luminescence and Applications, Changchun Institute of Optics, Fine Mechanics and Physics, Chinese Academy of Sciences, Changchun 130033, China; Center of Materials Science and Optoelectronics Engineering, University of Chinese Academy of Sciences, Beijing 100049, China;* orcid.org/0000-0002-1797-6857

**Shanli Zhang** − *State Key Laboratory of Luminescence and Applications, Changchun Institute of Optics, Fine Mechanics and Physics, Chinese Academy of Sciences, Changchun 130033, China; Center of Materials Science and Optoelectronics Engineering, University of Chinese Academy of Sciences, Beijing 100049, China*

**Zhiming Shi** − *State Key Laboratory of Luminescence and Applications, Changchun Institute of Optics, Fine Mechanics and Physics, Chinese Academy of Sciences, Changchun 130033, China; Center of Materials Science and Optoelectronics Engineering, University of Chinese Academy of Sciences, Beijing 100049, China;* orcid.org/0000-0002-1207-570X

**Jianwei Ben** − *State Key Laboratory of Luminescence and Applications, Changchun Institute of Optics, Fine Mechanics and Physics, Chinese Academy of Sciences, Changchun 130033, China; Center of Materials Science and Optoelectronics Engineering, University of Chinese Academy of Sciences, Beijing 100049, China*

**Ke Jiang** − *State Key Laboratory of Luminescence and Applications, Changchun Institute of Optics, Fine Mechanics and Physics, Chinese Academy of Sciences, Changchun 130033, China; Center of Materials Science and Optoelectronics Engineering, University of Chinese Academy of Sciences, Beijing 100049, China*

**Yuping Jia** − *State Key Laboratory of Luminescence and Applications, Changchun Institute of Optics, Fine Mechanics and Physics, Chinese Academy of Sciences, Changchun 130033, China; Center of Materials Science and Optoelectronics Engineering, University of Chinese Academy of Sciences, Beijing 100049, China*

**Mingrui Liu** − *State Key Laboratory of Luminescence and Applications, Changchun Institute of Optics, Fine Mechanics and Physics, Chinese Academy of Sciences, Changchun 130033, China; Center of Materials Science and Optoelectronics Engineering, University of Chinese Academy of Sciences, Beijing 100049, China*

**Dabing Li** − *State Key Laboratory of Luminescence and Applications, Changchun Institute of Optics, Fine Mechanics and Physics, Chinese Academy of Sciences, Changchun 130033, China; Center of Materials Science and Optoelectronics Engineering, University of Chinese Academy of Sciences, Beijing 100049, China;* orcid.org/0000-0001-5353-1460

Complete contact information is available at: https://pubs.acs.org/10.1021/acsami.2c10039


### Author Contributions

Y.C. carried out the Raman, XRD, AFM, SEM, PL, TEM, and EDX measurements; transferred the graphene film; designed the heat dissipation test of AlGaN epilayers; and wrote the article. H.Z. performed the theoretical calculations and analyzed the theoretical results. S.Z. designed the epitaxial procedure and performed the growth process of AlGaN epilayers by MOCVD. Z.S. provided the theoretical calculation method and supervised the theoretical results. J.B. performed the growth process of the low-temperature AlN layer by PVD. K.J., Y.J., and M.L. helped in the experimental data processing and result discussion. D.L. and X.S. designed the whole study; supervised the project; and revised the article.

### Notes

The authors declare no competing financial interest.



https://doi.org/10.1021/acsami.2c10039
ACS Appl. Mater. Interfaces 2022, 14, 37947−37957

## ■ ACKNOWLEDGMENTS

This work was supported by the National Key R&D Program of China (2019YFA0708202, 2021YFB3601600), the National Natural Science Foundation of China (61922078, 62121005, 61827813, 61874118, and 52002368), the Youth Innovation Promotion Association of the Chinese Academy of Sciences (Y201945 and 2019222), the Key Research Program of Frontier Sciences, Chinese Academy of Sciences (ZDBS-LY-JSC026), the Key Research Program of the Chinese Academy of Sciences (XDPB22), the Open Project of State Key Laboratory of Luminescence and Applications (E10932A2M1), the Key-Area Research and Development Program of Guangdong Province (2020B010169001), and the Suzhou Institute of Nano-Tech and Nano-Bionics (20YZ10).

## ■ REFERENCES

(1) Li, D. B.; Jiang, K.; Sun, X. J.; Guo, C. L. AlGaN Photonics: Recent Advances in Materials and Ultraviolet Devices. *Adv. Opt. Photonics* **2018**, *10*, 43−110.

(2) Amano, H.; Collazo, R.; Santi, C. D.; Einfeldt, S.; Funato, M.; Glaab, J.; Hagedorn, S.; Hirano, A.; Hirayama, H.; Ishii, R.; Kashima, Y.; Kawakami, Y.; Kirste, R.; Kneissl, M.; Martin, R.; Mehnke, F.; Meneghini, M.; Ougazzaden, A.; Parbrook, P. J.; Rajan, S.; Reddy, P.; Römer, F.; Ruschel, J.; Sarkar, B.; Scholz, F.; J Schowalter, L.; Shields, P.; Sitar, Z.; Sulmoni, L.; Wang, T.; Wernicke, T.; Weyers, M.; Witzigmann, B.; Wu, Y.-R.; Wunderer, T.; Zhang, Y. W. The 2020 UV Emitter Roadmap. *J. Phys. D: Appl. Phys.* **2020**, *53*, No. 503001.

(3) Hickman, A. L.; Chaudhuri, R.; Bader, S. J.; Nomoto, K.; Li, L.; Hwang, J. C. M.; Xing, H. G.; Jena, D. Next Generation Electronics on the Ultrawide-bandgap Aluminum Nitride Platform. *Semicond. Sci. Technol.* **2021**, *36*, No. 044001.

(4) Liu, S. F.; Luo, W.; Li, D.; Yuan, Y.; Tong, W.; Kang, J. J.; Wang, Y. X.; Li, D.; Rong, X.; Wang, T.; Chen, Z. Y.; Li, Y. D.; Wang, H. J.; Wang, W. Y.; Hoo, J.; Yan, L.; Guo, S. P.; Shen, B.; Cong, Z.; Wang, X. Q. Sec-Eliminating the SARS-CoV-2 by AlGaN Based High Power Deep Ultraviolet Light Source. *Adv. Funct. Mater.* **2021**, *31*, No. 2008452.

(5) Saito, Y.; Wada, S.; Nagata, K.; Makino, H.; Boyama, S.; Miwa, H.; Matsui, S.; Kataoka, K.; Narita, T.; Horibuchi, K. Efficiency Improvement of AlGaN-based Deep-ultraviolet Light-emitting Diodes and Their Virus Inactivation Application. *Jpn. J. Appl. Phys.* **2021**, *60*, No. 080501.

(6) Sharma, V. K.; Tan, S. T.; Zheng, H. Y.; Shendre, S.; Baum, A.; Chalvet, F.; Tirén, J.; Demir, H. V. On-Chip Mercury-Free Deep-UV Light-Emitting Sources with Ultrahigh Germicidal Efficiency. *Adv. Opt. Mater.* **2021**, *9*, No. 2100072.

(7) Muramoto, Y.; Kimura, M.; Kondo, A. Verification of Inactivation Effect of Deep-ultraviolet LEDs on Bacteria and Viruses, and Consideration of Effective Irradiation Methods. *Jpn. J. Appl. Phys.* **2021**, *60*, No. 090601.

(8) Lu, S. Q.; Zhong, Z. B.; Guo, B.; Chen, X. H.; Liu, G. Z.; Lin, Z. F.; Chen, H.; Huang, S. R.; Liang, X. D.; Zheng, Y. Z.; Huang, X. H.; Wang, M. X.; Xu, F. J.; Zhang, Y. H.; Zhang, C. M.; Wang, X. D.; Zhou, Y. H.; Li, S. P.; Lee, J. K.; Cai, D. J.; Kang, J. Y. Unidirectional Elimination of Hydrogen by a Giant Local Field Saves First- and Last-Mile Performances of Semiconductor Devices. *J. Phys. Chem. Lett.* **2022**, *13*, 2084−2093.

(9) Kneissl, M.; Seong, T.-Y.; Han, J.; Amano, H. The Emergence and Prospects of Deep-ultraviolet Light-emitting Diode Technologies. *Nat. Photonics* **2019**, *13*, 233−244.

(10) Hagedorn, S.; Walde, S.; Knauer, A.; Susilo, N.; Pacak, D.; Cancellara, L.; Netzel, C.; Mogilatenko, A.; Hartmann, C.; Wernicke, T.; Kneissl, M.; Weyers, M. Status and Prospects of AlN Templates on Sapphire for Ultraviolet Light-Emitting Diodes. *Phys. Status Solidi A* **2020**, *217*, No. 1901022.

(11) Chen, L.; Lin, W.; Wang, H. Q.; Li, J. C.; Kang, J. Y. Reversing Abnormal Hole Localization in High-Al-content AlGaN Quantum Well to Enhance Deep Ultraviolet Emission by Regulating the Orbital State Coupling. *Light: Sci. Appl.* **2020**, *9*, No. 104.

(12) Cai, Q.; You, H. F.; Guo, H.; Wang, J.; Liu, B.; Xie, Z. L.; Chen, D. J.; Lu, H.; Zheng, Y. D.; Zhang, R. Progress on AlGaN-based Solar-blind Ultraviolet Photodetectors and Focal Plane Arrays. *Light: Sci. Appl.* **2021**, *10*, No. 94.

(13) Yoshida, H.; Kimura, S. High-crystalline-quality AlN Grown on SiC Substrates by Controlling Growth Mode. *J. Cryst. Growth* **2020**, *537*, No. 125605.

(14) Zheng, Y.; Agrawal, M.; Dharmarasu, N.; Radhakrishnan, K.; Patwal, S. A study on Ga-Si Interdiffusion During (Al)GaN/AlN Growth on Si by Plasma Assisted Molecular Beam Epitaxy. *Appl. Surf. Sci.* **2019**, *481*, 319−326.

(15) Yin, X.; Zhao, S. R. High Internal Quantum Efficiency AlGaN Epilayer Grown by Molecular Beam Epitaxy on Si Substrate. *ECS J. Solid State Sci. Technol.* **2021**, *10*, No. 076001.

(16) Lee, S.-M.; Choi, W.; Kim, J.; Kim, T.; Lee, J.; Im, S. Y.; Kwon, J. Y.; Seo, S.; Shin, M.; Moon, S. E. Thermal Conductivity and Thermal Boundary Resistances of ALD Al2O3 Films on Si and Sapphire. *Int. J. Thermophys.* **2017**, *38*, No. 176.

(17) Tye, R. P. Preliminary Measurements on the Thermal and Electrical Conductivities of Molybdenum, Niobium, Tantalum and Tungsten. *J. Less-Common Met.* **1961**, *3*, 13−18.

(18) Chung, J. W.; Piner, E. L.; Palacios, T. N-Face GaN/AlGaN HEMTs Fabricated Through Layer Transfer Technology. *IEEE Electron. Device Lett.* **2009**, *30*, 113−116.

(19) Sergent, S.; Arita, M.; Kako, S.; Tanabe, K.; Iwamoto, S.; Arakawa, Y. High-Q AlN Ladder-Structure Photonic Crystal Nanocavity Fabricated by Layer Transfer. *Phys. Status Solidi C* **2013**, *10*, 1517−1520.

(20) Wang, Q.; Liang, Z. W.; Wang, Q.; Zhang, G. Y. Fabrication of a Thermostable Ga-face GaN Template on a Molybdenum Substrate via Layer Transfer. *Opt. Mater. Express* **2020**, *10*, 2447−2455.

(21) Yamada, K.; Asahi, H.; Tampo, H.; Imanishi, Y.; Ohnishi, K.; Asami, K. Strong Photoluminescence Emission from Polycrystalline GaN Layers Grown on W, Mo, Ta, and Nb Metal Substrates. *Appl. Phys. Lett.* **2001**, *78*, No. 2849.

(22) Okamoto, K.; Inoue, S.; Matsuki, N.; Kim, T.-W.; Ohta, J.; Oshima, M.; Fujioka, H.; Ishii, A. Epitaxial Growth of GaN Films Grown on Single Crystal Fe Substrates. *Appl. Phys. Lett.* **2008**, *93*, No. 251906.

(23) Wang, W. L.; Yang, W. J.; Liu, Z. L.; Lin, Y. H.; Zhou, S. Z.; Qian, H. R.; Gao, F. L.; Li, G. Q. Epitaxial Growth of High Quality AlN Films on Metallic Aluminum Substrates. *CrystEngComm* **2014**, *16*, 4100−4107.

(24) Wang, W. L.; Yang, W. J.; Liu, Z. L.; Lin, Y. H.; Zhou, S. Z.; Qian, H. R.; Gao, F. L.; Yang, H.; Li, G. Q. Epitaxial Growth of Homogeneous Single-crystalline AlN Films on Single-crystalline Cu (111) Substrates. *Appl. Surf. Sci.* **2014**, *294*, 1−8.

(25) Wang, W. L.; Yang, W. J.; Liu, Z. L.; Lin, Y. H.; Zhou, S. Z.; Qian, H. R.; Wang, H. Y.; Lin, Z. T.; Li, G. Q. Epitaxial Growth of High-quality AlN Films on Metallic Nickel Substrates by Pulsed Laser Deposition. *RSC Adv.* **2014**, *4*, 27399−27403.

(26) Chen, Y.; Zang, H.; Jiang, K.; Ben, J. W.; Zhang, S. L.; Shi, Z. M.; Jia, Y. P.; Lü, W.; Sun, X. J.; Li, D. B. Improved Nucleation of AlN on *in situ* Nitrogen Doped Graphene for GaN Quasi-van der Waals Epitaxy. *Appl. Phys. Lett.* **2020**, *117*, No. 051601.

(27) Chen, Y.; Shi, Z. M.; Zhang, S. L.; Ben, J. W.; Jiang, K.; Zang, H.; Jia, Y. P.; Lü, W.; Li, D. B.; Sun, X. J. The van der Waals Epitaxy of High-Quality N-Polar Gallium Nitride for High-Response Ultraviolet Photodetectors with Polarization Electric Field Modulation. *Adv. Electron. Mater.* **2021**, *8*, No. 2100759.

(28) Suk, J. W.; Kitt, A.; Magnuson, C. W.; Hao, Y. F.; Ahmed, S.; An, J.; Swan, A. K.; Goldberg, B. B.; Ruoff, R. S. Transfer of CVD-Grown Monolayer Graphene onto Arbitrary Substrates. *ACS Nano* **2011**, *5*, 6916−6924.

(29) Wang, H.; Wang, G. Z.; Bao, P. F.; Yang, S. L.; Zhu, W.; Xie, X.; Zhang, W.-J. Controllable Synthesis of Submillimeter Single-

Crystal Monolayer Graphene Domains on Copper Foils by Suppressing Nucleation. *J. Am. Chem. Soc.* **2012**, *134*, 3627−3630.
(30) Achra, S.; Wu, X. Y.; Trepalin, V.; Nuytten, T.; Ludwig, J.; Afanas'ev, V.; Brems, S.; Sorée, B.; Tokei, Z.; Heyns, M.; Asselberghs, I. Metal Induced Charge Transfer Doping in Graphene-ruthenium Hybrid Interconnects. *Carbon* **2021**, *183*, 999−1011.
(31) Chen, Y.; Fu, X. Y.; Yue, Y. Y.; Zhang, N.; Feng, J.; Sun, H. B. Flexible and Transparent Supercapacitor Based on Ultrathin Au/graphene Composite Electrodes. *Appl. Surf. Sci.* **2019**, *467*−*468*, 104−111.
(32) Tanaka, Y.; Hasebe, Y.; Inushim, T.; Sandhu, A.; Ohoya, S. Comparison of AlN Thin Films Grown on Sapphire and Cubic-SiC Substrates by LP-MOCVD. *J. Cryst. Growth* **2000**, *209*, 410−414.
(33) Matsumoto, T.; Kiuchi, M. Zinc-blende Aluminum Nitride Formation Using Low-energy Ion Beam Assisted Deposition. *Nucl. Instrum. Methods Phys. Res., Sect. B* **2006**, *242*, 424−426.
(34) Chen, Z. L.; Liu, Z. Q.; Wei, T. B.; Yang, S. Y.; Dou, Z. P.; Wang, Y. Y.; Ci, H. N.; Chang, H. L.; Qi, Y.; Yan, J. C.; Wang, J. X.; Zhang, Y. F.; Gao, P.; Li, J. M.; Liu, Z. F. Improved Epitaxy of AlN Film for Deep-Ultraviolet Light-Emitting Diodes Enabled by Graphene. *Adv. Mater.* **2019**, *31*, No. 1807345.
(35) Ning, J.; Yan, C. C.; Jia, Y. Q.; Wang, B. Y.; Zeng, Y.; Zhang, J. C.; Wang, D.; Hao, Y. GaN Films Deposited on Sapphire Substrates Sputter-Coated with AlN Followed by Monolayer Graphene for Solid-State Lighting. *ACS Appl. Nano Mater.* **2020**, *3*, 5061−5069.
(36) Pang, W. Y.; Lo, I.; Wu, S.; Lin, Z. X.; Shih, C. H.; Lin, Y. C.; Wang, Y. C.; Hu, C. H.; Hsu, G. Z. L. Growth of Wurtzite and Zinc-blende Phased GaN on Silicon (100) Substrate with Sputtered AlN Buffer Layer. *J. Cryst. Growth* **2013**, *382*, 1−6.
(37) Petrov, I.; Mojab, E.; Powell, R. C.; Greene, J. E.; Hultman, L.; Sundgren, J. E. Synthesis of Metastable Epitaxial Zinc-blende-structure AlN by Solid-state Reaction. *Appl. Phys. Lett.* **1992**, *60*, No. 2491.
(38) Chen, Y.; Zhang, N.; Li, Y. F.; Bi, Y. G.; Yue, Y. Y.; Feng, J.; Sun, H. B. Microscale-Patterned Graphene Electrodes for Organic Light-Emitting Devices by a Simple Patterning Strategy. *Adv. Opt. Mater.* **2018**, *6*, No. 1701348.
(39) Kresse, G.; Furthmüller, J. Efficient Iterative Schemes for ab Initio Total-energy Calculations Using a Plane-wave Basis Set. *Phys. Rev. B* **1996**, *54*, 11169−11186.
(40) Kresse, G.; Furthmüller, J. Efficiency of ab-initio Total Energy Calculations for Metals and Semiconductors Using a Plane-wave Basis Set. *Comput. Mater. Sci.* **1996**, *6*, 15−50.
(41) Blöchl, P. E. Projector Augmented-wave Method. *Phys. Rev. B* **1994**, *50*, 17953−17979.
(42) Kresse, G.; Joubert, D. From Ultrasoft Pseudopotentials to the Projector Augmented-wave Method. *Phys. Rev. B* **1999**, *59*, 1758−1775.
(43) Perdew, J. P.; Burke, K.; Ernzerhof, M. Generalized Gradient Approximation Made Simple. *Phys. Rev. Lett.* **1996**, *77*, 3865−3868.
(44) Grimme, S.; Antony, J.; Ehrlich, S.; Krieg, H. A Consistent and Accurate ab Initio Parametrization of Density Functional Dispersion Correction (DFT-D) for the 94 Elements H-Pu. *J. Chem. Phys.* **2010**, *132*, No. 154104.




https://doi.org/10.1021/acsami.2c10039
*ACS Appl. Mater. Interfaces* 2022, 14, 37947−37957